ACS Energy LETTERS

http://pubs.acs.org/journal/aelccp

LETTER

Heterogeneous Cation−Lattice Interaction and Dynamics in Triple-Cation Perovskites Revealed by Infrared Vibrational Nanoscopy

Jun Nishida, Amani H. Alfaifi, Thomas P. Gray, Sean E. Shaheen, and Markus B. Raschke*

Cite This: *ACS Energy Lett.* 2020, 5, 1636−1643

Read Online

ACCESS | Metrics & More | Article Recommendations | Supporting Information

ABSTRACT: Hybrid organic−inorganic perovskites exhibit extraordinary photovoltaic performance. This is believed to arise from almost liquid-like low-energy interactions among lattice ions and charge carriers. While spatial variations have recently been identified over multiple length scales in the optoelectronic response of perovskites, the relationship between the heterogeneity and the soft cation−lattice interactions has remained elusive. Here, we apply multivariate infrared vibrational nanoimaging to a formamidinium (FA)−methylammonium (MA)−cesium triple-cation perovskite by using the FA vibrational resonance as a sensitive probe of its local chemical environment. The derived correlation among nanoscale composition, cation−lattice coupling, and associated few-picosecond vibrational dynamics implies a heterogeneous reaction field and lattice contraction that we attribute to a spatially nonuniform distribution of cesium cations. The associated spatial variation in elasticity of the lattice leads to disorder in charge−phonon coupling and related polaron formation—the control of which is central to improving perovskite photovoltaics.

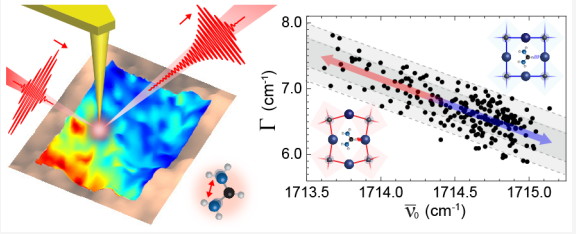

Hybrid organic−inorganic perovskites have been intensely studied in recent years for their remarkable photovoltaic performance.[1−6] One of the core properties underlying the photophysical response of perovskites is their unusually dynamic lattice. The associated cation−lattice interaction is determined by organic cations rotating and switching hydrogen-bonding sites on ultrafast time scales[7−15] and the soft inorganic framework undergoing low-frequency vibrations in the terahertz regime.[16−19] The dynamic lattice is believed to play a central role in stabilizing the photoinduced carriers, by a reconfiguration of the surrounding lattice and polaron formation.[20−22] However, the associated overall weak chemical bonding within the structure conversely results in chemical instability, most notoriously in the presence of atmospheric humidity and oxygen.[23−25] Precise tuning of cation−lattice interactions and coupled lattice dynamics is therefore key to understanding and simultaneously enhancing optoelectronic performance and chemical stability. In a variety of efforts to control the dynamic lattice response, compositional engineering has proven successful by incorporating cations and anions with different ionic radii and field strengths into the perovskite lattice.[26−31]

Unlike conventional inorganic semiconductor-based photovoltaics, spin-coated perovskite films exhibit spatial heterogeneity in open-circuit voltage, bandgap, and photoluminescence intensity and lifetime, as found in recent studies by scanning probe and photoluminescence microscopy.[32−52] Interestingly, the optoelectronic response in perovskites seem to vary over multiple length scales, from nanometer subgranular, to grain-to-grain, and further into micrometer scales across multiple grains,[32] suggesting the contributions of more than one physical mechanism controlling the disorder and thus device performance. However, the characterization of the associated spatial variations of the elementary cation−lattice interaction has remained limited.

The spatially resolved characterization of the cation−lattice interactions and their coupling and dynamics requires simultaneous implementation of imaging with spatial resolution beyond the homogeneous domain size limit and spectroscopic access into the low-energy landscape of the perovskite lattice. While infrared vibrational nanospecteroscopy[47,48,52] and X-ray fluorescence microscopy[38] have successfully elucidated compositional heterogeneity with high spatial resolution and chemical specificity, insights into the variations of the critical cation−

Received: March 5, 2020
Accepted: April 9, 2020
Published: April 9, 2020

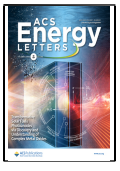

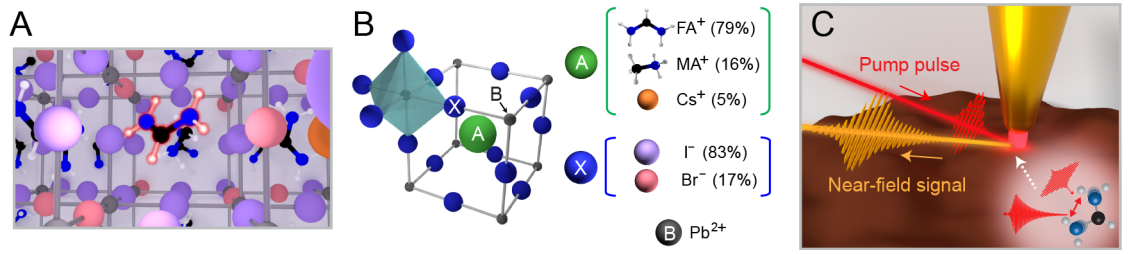

Figure 1. Infrared vibrational nanospectroscopy of a triple-cation perovskite. (A) The dynamic lattice of the triple-cation perovskite FAMACs with the formamidinium cation (FA^+, center) serving as a local probe of the cation−lattice interaction through its vibrational resonance. (B) The chemical composition and unit cell structure of the FAMACs perovskite, $[(FA_{0.83}MA_{0.17})_{0.95}Cs_{0.05}]Pb(I_{0.83}Br_{0.17})_3$. (C) Schematic illustration of IR *s*-SNOM experiment, where the nano-localized near-field formed by the input mid-infrared pulse interacts with the FAMACs perovskite, scattering the signal field encoding the vibrational free induction decay (FID) from the CN antisymmetric stretch mode of the FA^+ cation.

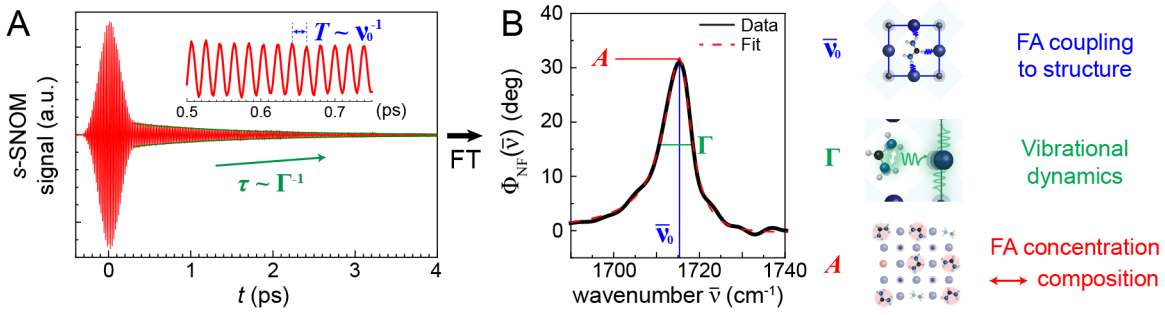

Figure 2. Nano-localized vibrational signal in time and frequency. (A) Infrared vibrational *s*-SNOM interferogram of the FAMACs perovskite film measured by interfering a scattered near-field signal with a reference field, with the vibrational FID observed as a long-lasting coherence. (B) The phase spectrum in frequency domain arising from Fourier transform of the corresponding time-domain interferogram, shown together with the fitting curve based on Lorentzian vibrational resonance and point dipole model (PDM). The spatial variations in the peak area (*A*), peak position ($\bar{\nu}_0$), and line width (Γ) report on the heterogeneity in terms of the concentration of the FA^+ cation, the cation−lattice interaction, and their associated vibrational dynamics, respectively.

lattice coupling have remained elusive because of the difficulty to spectrally resolve the low-energy interaction.

Here, we use infrared nanospectroscopic imaging based on scattering scanning near-field optical microscopy (IR *s*-SNOM) to probe the vibrational resonance of the formamidinium cation, which acts as a reporter of its local chemical environments in the triple-cation perovskite $[(FA_{0.83}MA_{0.17})_{0.95}Cs_{0.05}]Pb(I_{0.83}Br_{0.17})_3$, termed FAMACs (Figure 1A) with formamidinium (FA), methylammonium (MA), and cesium (Cs) mixed as A-site cations (Figure 1B). By measuring the nano-localized vibrational resonance with high precision, we resolve subtle spatial variations in the vibrational line shape. This allows us to go beyond conventional chemical mapping and characterize the spatial heterogeneity and correlations in composition, cation−lattice interaction, and its dynamics. Insight into this dynamic coupling helps understanding the nonuniformity in the fundamental low-energy processes in this model perovskite system, which is chosen for its high stability against humidity together with an optimal bandgap for solar cell applications.[27,29]

The spatio-spectral IR *s*-SNOM imaging of the FA cation's CN antisymmetric stretch mode provides for a spatially resolved mapping of composition within a spin-coated FAMACs film. Furthermore, with subwavenumber (<0.1 meV) precision resolved variations in vibrational peak position and line width, we are able to probe disorder in the cation−lattice interactions and their coupled vibrational dynamics.[53−57] To study the evolution of heterogeneity induced by an external perturbation, we expose the perovskite film to high humidity that results in the formation of larger vapor-annealed grains as previously observed in different perovskites,[58] yet surprisingly with no correlated change in chemical heterogeneity. We observe that stronger cation−lattice interactions facilitate vibrational damping, suggesting a varying degree of lattice contraction potentially due to a nonuniform distribution of cesium cations. The observed variations in the low-energy landscape likely give rise to disordered charge−phonon coupling and subsequent polaron formation, which regulate the optoelectronic responses of perovskites.

FAMACs Perovskite. Spin-coated films of triple-cation perovskite FAMACs with the average chemical formulation of $[(FA_{0.83}MA_{0.17})_{0.95}Cs_{0.05}]Pb(I_{0.83}Br_{0.17})_3$ (Figure 1B) are prepared by following a procedure by Saliba et al.,[27] yielding as-prepared films of ∼600 nm thickness and ∼100 nm average grain size with a broad size distribution between 50−200 nm as typically observed previously.[52] Water-vapor annealed films with larger grain sizes are obtained by exposing the film to 90% RH for 36 h. See the Supporting Information for further details on sample preparation and characterization.

IR s-SNOM. IR *s*-SNOM nano-Fourier transform infrared (nano-FTIR) spectroscopic imaging is performed by illuminating the tip of a tapping mode atomic force microscope (nanoIR2-s, prototype, Anasys Instruments/Bruker) with femtosecond infrared radiation[54] (for details, see the Supporting Information, Figure S2). The infrared pulse with the center frequency of ∼1715 cm^{-1} and the spectral bandwidth of ∼100 cm^{-1} fwhm (Flint, Light Conversion; Levante OPO + HarmoniXX DFG, APE GmbH) provides low noise and high spectral irradiance to characterize the CN antisymmetric stretch

https://dx.doi.org/10.1021/acsenergylett.0c00522
ACS Energy Lett. 2020, 5, 1636−1643

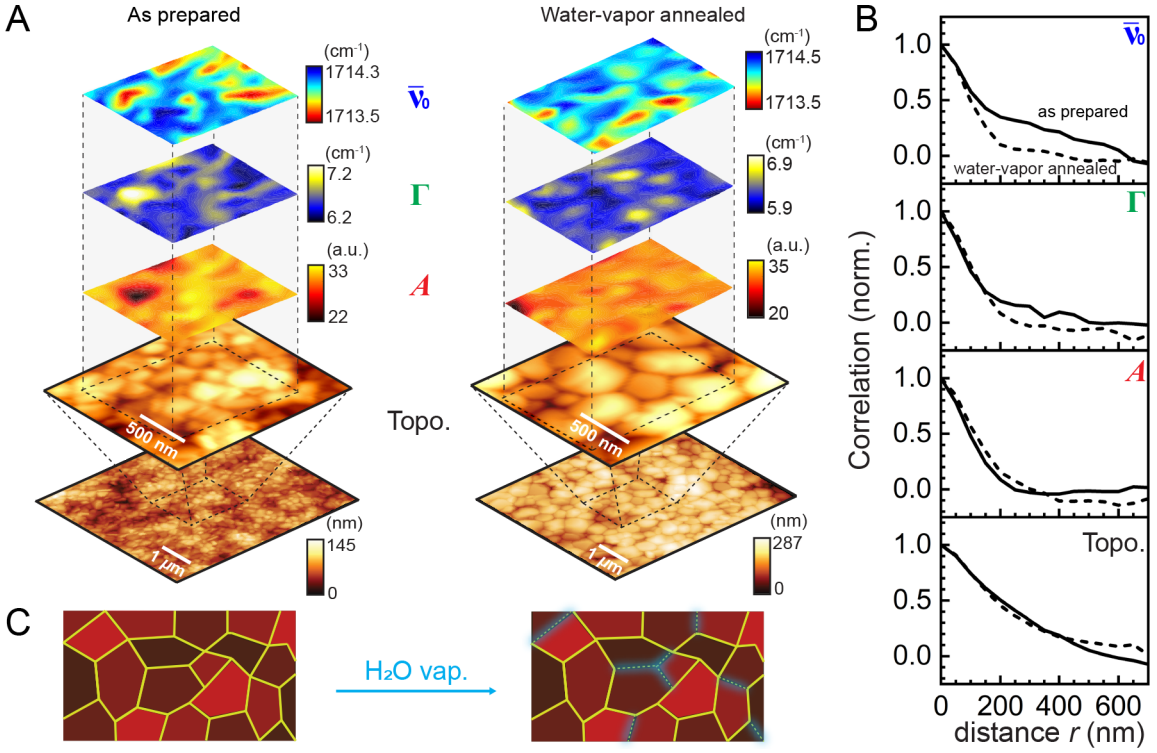

Figure 3. (A) Vibrational infrared *s*-SNOM imaging of the FAMACs perovskite film as prepared (left) and the film annealed by high humidity (right), with a clear signature of spatial variations in the peak area (A), peak positions ($\bar{\nu}_0$), and line width (Γ) corresponding to compositional, structural, and dynamical heterogeneity. The IR *s*-SNOM images are constructed by cubic splining based on 100 data points within the regions indicated by the dotted squares in the corresponding AFM topography images. (B) The radial autocorrelations of each vibrational *s*-SNOM parameter based on multiple data sets. Regardless of the larger grain sizes in the water-vapor annealed film, the correlation lengths for the vibrational *s*-SNOM parameters do not evolve accordingly, suggesting the formation of subgrain heterogeneity. (C) The mechanism of the subgrain heterogeneity formation, where the grains fuse only at their boundaries while retaining heterogeneous domains associated with the original grains.

mode of FA cations (Figure 1C). The high spectral irradiance enables selective vibrational mode excitation and spectroscopy with high signal-to-noise ratio, allowing for precise line-shape analysis as a measure for molecular coupling and dynamics. This is in contrast to broadband synchrotron infrared nanospectroscopy (SINS),[52,59] which can simultaneously characterize multiple vibrational resonances spanning a wide spectral range,[60] yet with limited signal-to-noise for each resonance because of the low spectral irradiance of synchrotron IR.

The gold-coated AFM tip serves as an optical dipole antenna, and the tip-scattered localized near-field vibrational response is observed through interferometric optical heterodyne detection. Figure 2A shows a typical nano-IR interferogram for a FAMACs as-prepared perovskite film. The free-induction decay (FID) signal, following the broadband instantaneous nonresonant response, already indicates the long dephasing time of the FA vibration. Fourier transform then yields dispersive amplitude $A_{NF}(\bar{\nu})$ and absorptive phase $\Phi_{NF}(\bar{\nu})$ spectra, corresponding to the complex refractive index $\tilde{n}(\bar{\nu}) = n(\bar{\nu}) + i\kappa(\bar{\nu})$ with dispersion $n(\bar{\nu})$ and absorption $\kappa(\bar{\nu})$ to good approximation.[54] Assuming a Lorentzian vibrational resonance and modeling the frequency-dependent scattering using the established point dipole model, the observed asymmetric line shape in $\Phi_{NF}(\bar{\nu})$ is reproduced with the vibrational peak area (A), peak position ($\bar{\nu}_0$), and line width (Γ) as fitting parameters (Figure 2B). While the absolute values of the retrieved parameters are somewhat dependent on the model details of the near-field tip−sample interaction,[54,55,57] we find the extracted spatial variations and correlations to be consistent across the different models as delineated in the Supporting Information (Figures S3 and S4).

The localization of the IR *s*-SNOM signal is determined to first order by the apex radius of the tip, which is ∼20 nm. The corresponding spatial resolution allows for probing grain-to-grain heterogeneity in as-prepared samples and subgrain heterogeneity in water-vapor annealed films, as discussed below.

Vibrational Nanoimaging. Figure 3A (left) shows the spatial variation of peak area (A), peak position ($\bar{\nu}_0$), and line width (Γ), together with the AFM topography image reflecting the polycrystalline nature of the as-prepared FAMACs film. To extract the length scale of the spatial variation, the radial autocorrelations of each *s*-SNOM image are calculated (Figure 3B, solid lines). As can be seen, while the correlation length for the peak area A agrees with the grain size of ∼100 nm from the topography, $\bar{\nu}_0$ and Γ vary over longer length scales than individual grain sizes.

We next study water-vapor annealed films (Figure 3A, right). The AFM topography image shows larger perovskite grains (>200 nm), suggesting that the high humidity annealed the perovskite grains, similar to previous observations for an $MAPbI_3$ perovskite.[58] In spite of the larger grain sizes, in the corresponding radial autocorrelations (Figure 3B, dotted lines), the correlation length for all three parameters of A, $\bar{\nu}_0$, and Γ are nearly identical and shorter than those observed in the as-prepared film.

We interpret the spatial variation of the vibrational parameters in terms of cation composition and cation−lattice interaction.

https://dx.doi.org/10.1021/acsenergylett.0c00522
ACS Energy Lett. 2020, 5, 1636−1643

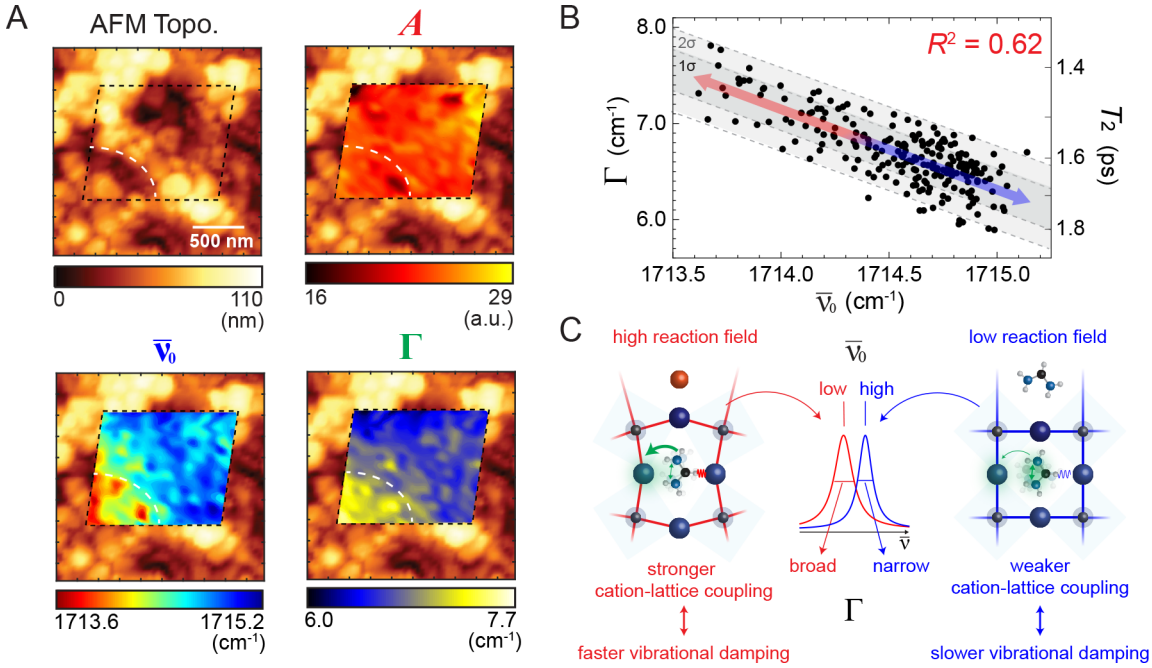

Figure 4. Vibrational peak position−line-width correlation. (A) Representative IR *s*-SNOM vibrational images exhibiting a strong anticorrelation between the peak position and line width, together with the spatial correlation. (B) The corresponding peak position ($\bar{\nu}_0$)−line width (Γ) correlation plot, with the line width converted to the dephasing time T_2. (C) A potential microscopic mechanism behind the $\bar{\nu}_0$−Γ anticorrelation, caused by the variation in cesium concentration. Higher cesium concentration contracts the lattice structure (left), resulting in stronger cation−lattice interaction and faster vibrational damping. Lower cesium concentration expands the lattice (right) and yields weaker cation−lattice interaction and slower vibrational damping.

The peak area (A) reflects the concentration of the FA cation within the nano-localized excitation volume, thus probing compositional heterogeneity within a film. Further, infrared vibrational peak positions ($\bar{\nu}_0$) have been established to be sensitive to local interactions between probe molecules and surrounding chemical environments, as demonstrated for multiple molecular vibrational resonances in a variety of materials and attributed to, for example, a vibrational Stark effect.[61,62] In our case, the variation in the peak position $\bar{\nu}_0$ signifies varying cation−lattice interactions arising from spatially heterogeneous lattice structures within perovskite, where a stronger cation−lattice interaction yields a red-shifted peak position due to a locally higher reaction field. Lastly, although multiple contributions including homogeneous and inhomogeneous broadening affect the vibrational line width (Γ),[63] the line width of the CN antisymmetric stretch mode of the FA cation is mostly dominated by homogeneous broadening, as suggested by a recent far-field two-dimensional infrared (2D IR) study on similar perovskites.[14,15] Our reproduction of the measured near-field spectra $\Phi_{NF}(\bar{\nu})$ with Lorentzian vibrational line shapes to good approximation indeed supports the interpretation of homogeneous broadening. Observed variations in the line width can thus be quantitatively converted to variations in the corresponding dephasing time ($T_2 \propto 1/\Gamma$) and used as a measure of the associated cation−lattice coupled vibrational dynamics.

In the as-prepared film, the variation in the peak area A, with a correlation length similar to the grain dimensions, reveals varying composition in A-site cation from grain to grain. In contrast, the variations in the peak position ($\bar{\nu}_0$) and line width (Γ) at a length scale exceeding the grain sizes suggest that the structures and dynamics of neighboring grains tend to be correlated. Such long correlation length exceeding grain sizes points to a possible film growth mechanism, where a grain formed earlier serves as a template or nucleation site for the formation of adjacent grains. A similar behavior has been previously observed in the formation of molecular semiconductor crystals, where orientations of the molecular crystals correlate over a longer length scale than grain dimensions.[60]

The observed spatial variation in peak position $\bar{\nu}_0$ should contribute to the infrared absorption band as inhomogeneous broadening when characterized in ensemble-averaged far-field measurements. Interestingly, while the CN antisymmetric mode of the FA cation in $FAPbI_3$ perovskite is largely homogeneously broadened,[14] a 2D IR spectrum for the same vibrational mode in a mixed cation perovskite exhibits a signature of a small but non-negligible contribution from inhomogeneous broadening.[15] Thus, at least a fraction of such contribution from the inhomogeneous broadening should be attributed to the nanoscale spatial heterogeneity in the peak position $\bar{\nu}_0$ observed here.

Water-Vapor Annealing. In contrast, for water-vapor annealed grains, correlation lengths shorter than grain sizes reveal a subgrain heterogeneity. This behavior can be reasonably explained by an expected formation mechanism of the water-vapor annealed grains, where grains fuse only at their boundaries without homogenizing the heterogeneous bulk domains associated with the original grains, as illustrated in Figure 3C. The reduced correlation lengths for $\bar{\nu}_0$ and Γ, compared with those for the film as prepared, might arise from the fused grain boundaries with irregular structures and dynamics, as suggested by the blurred domains in Figure 3C.

The humidity-induced annealing stands in clear contrast to thermally induced degradation, where the formation of PbI_2 is observed through the complete loss of the FA vibrational resonance in the same triple-cation perovskite using broadband

https://dx.doi.org/10.1021/acsenergylett.0c00522
ACS Energy Lett. 2020, 5, 1636−1643

IR *s*-SNOM.[52] The lack of evolution in the FA vibrational resonance upon water-vapor annealing, together with a maintained band structure of the perovskite (see the Supporting Information), confirms a preserved cubic perovskite phase and verifies solvent-vapor annealing to be a potential tool to control the granularity of perovskites.[58,64,65] The subgrain heterogeneity in the annealed grains could lead to unique transport properties of carriers and associated polarons due to the structural and dynamical mismatch across neighboring vapor-annealed domains.

Correlation between Reaction Field and Vibrational Damping. To address the physical mechanism leading to the observed variations in $\bar{\nu}_0$ and Γ, we create correlation plots among the three vibrational parameters (A, $\bar{\nu}_0$, and Γ). The absence of correlations between $A-\bar{\nu}_0$ or $A-\Gamma$ (Figure S5) indicates that a varying concentration of the FA cation is not a dominant mechanism in regulating lattice structure and dynamics. In contrast, a negative correlation between peak position $\bar{\nu}_0$ and line width Γ (Figure 4A,B) for the as-prepared film suggests that the corresponding strength of cation−lattice interactions and their associated vibrational dynamics vary together in a concerted manner. We also observe a similar correlation for the water-vapor annealed film (Figure S5), suggesting that a common microscopic mechanism underlies the structural and dynamical nonuniformity in both cases.

The negative correlation between $\bar{\nu}_0$ and Γ is consistent with related observations, most prominently in hydrogen bonded systems, allowing us to infer the underlying microscopic mechanism.[53,61,66,67] The correlation observed can be explained by two distinct features of the vibrational dynamics in mixed cation perovskites, namely, (i) a nonuniform cation−lattice coupling due to a varying extent of lattice contraction[28] that facilitates the cation-to-lattice vibrational damping and (ii) a homogeneously broadened line width of the FA vibrational resonance purely reflecting the vibrational dephasing dynamics pertaining to the cation−lattice interaction.[14] This implies that a stronger lattice contraction imposes a more intense reaction field on the FA cation inducing a red-shift in the peak position ($\bar{\nu}_0$),[68] while it simultaneously leads to a faster cation-to-lattice vibrational damping rate that broadens the homogeneous line width (Γ) (Figure 4C).

A minor doping (<5%) of cesium, which has a much smaller ionic radius than the FA and MA cations, not only significantly contracts the crystal lattice but also slows the lattice dynamics, as represented by an extended reorientation time of the FA cation as suggested recently.[28] This lattice contraction mechanism can explain the observed negative peak position−line width correlation, by assuming that the spatial variations in these parameters result from a variation in cesium concentration (Figure 4C). Higher cesium concentration contracts the lattice, which creates a higher reaction field as experienced by the FA cations, resulting in a vibrational red-shift due to a vibrational Stark effect. The contracted lattice also slows the rotational dynamics of the cation and enforces a stronger cation−lattice coupling, facilitating the cation-to-lattice vibrational damping which results in a faster dephasing time. In contrast, the FA cations in domains with lower cesium content experience a lower reaction field due to a more expanded lattice structure and thus a weaker cation−lattice coupling, resulting in a blue-shift together with a slower dephasing time. Considering the nonuniform concentration of FA cation together with the previously reported heterogeneous halide composition,[38] such disordered cesium distribution is likely present in mixed cation perovskites. This is also supported by a ^{133}Cs NMR study revealing inhomogeneously broadened line shapes in mixed cation perovskites.[69]

Considering the major roles that the cesium cation is believed to play in mixed cation perovskites,[28,30,31] the nonuniform distribution of cesium cations is likely a cause of the heterogeneous lattice contraction as discussed above. While the disorder in the anion composition could in principle cause the varying degree of lattice contraction as well, the difference in the effective ionic radii between Br^- (196 pm) and I^- (220 pm) is much smaller than the mismatch in the radius of Cs^+ (167 pm) from those of the other cations (253 pm for FA^+ and 217 pm for MA^+).[70,71] Thus, the variation in the cesium concentration likely leads to more pronounced impact on the lattice contraction compared with that of the anion distribution. The observed correlation thus reveals the structural heterogeneity originating from the unique nature of the highly elastic lattice of perovskites, which is believed to exhibit extreme sensitivity to subtle variations in A-site cation composition.[28]

The spatial heterogeneity that we identify in cation−lattice interactions provides important implications for understanding the previously observed chemical and optoelectronic heterogeneity in perovskites. The chemical stability of perovskites is highly dependent on their composition.[26,27] Therefore, the heterogeneous composition observed here would lead to varying stability within the film, with the presence of more reactive domains that can act as seeds for larger-scale degradation (Figure S1A).[72−74]

The spatially varying cation−lattice couplings, manifested by heterogeneous lattice contraction, affect the local elasticity of the perovskite lattice. Upon the generation of photoinduced carriers, this leads to disordered charge−phonon coupling and associated polaron formation, which involves the dynamical reconfiguration of the lattice structure surrounding a charge. Considering the widely accepted roles of the polaron in determining the optoelectronic responses of perovskites,[16,17,20] such polaron heterogeneity likely accounts for previously reported optoelectronic disorders within perovskites.[32−46,52]

In summary, using vibrational spectroscopic nanoimaging with high precision, we resolved the spatial heterogeneity in the fundamental low-energy interaction in a model organic−inorganic hybrid perovskite. The line-shape analysis of the vibrational response provides insights into the nonuniform cation−lattice interaction and its dynamics. In triple-cation perovskite films, we resolved heterogeneity in the cation−lattice coupling at grain-to-grain and larger length scales. Subgrain heterogeneity observed in a water-vapor annealed film suggests an annealing mechanism in which grains fuse only at their boundaries without significant cation diffusion. The correlated cation−lattice coupling and associated vibrational relaxation together yield a microscopic picture of the nonuniform lattice deformation across the film. The varying degree of lattice contraction leads to heterogeneous polaron formation and mobility, which act as a regulating mechanism behind spatially varying optoelectronic properties of the perovskites.[32]

Our approach of multivariate infrared vibrational nanospectroscopy is generally applicable to the wide variety of other hybrid perovskites with molecular cations and anions. The heterogeneity in fundamental low-energy interactions and coupling, characterized by hyperspectral infrared vibrational nanoimaging, can thus facilitate the understanding and control of disorder toward the further enhancement of the photovoltaic performance of perovskites.

https://dx.doi.org/10.1021/acsenergylett.0c00522
ACS Energy Lett. 2020, 5, 1636−1643

■ ASSOCIATED CONTENT

Supporting Information

The Supporting Information is available free of charge at https://pubs.acs.org/doi/10.1021/acsenergylett.0c00522.

(A) Synthesis and characterization of the FAMACs perovskite, (B) detailed description of the IR *s*-SNOM system, (C) tip−sample near-field interaction, and (D) correlations among all the vibrational parameters (PDF)

■ AUTHOR INFORMATION

Corresponding Author

Markus B. Raschke − *Department of Physics, Department of Chemistry, and JILA, University of Colorado, Boulder, Colorado 80309, United States;* orcid.org/0000-0003-2822-851X; Email: markus.raschke@colorado.edu

Authors

Jun Nishida − *Department of Physics, Department of Chemistry, and JILA, University of Colorado, Boulder, Colorado 80309, United States;* orcid.org/0000-0001-7834-8179

Amani H. Alfaifi − *Department of Mechanical and Material Engineering, University of Denver, Denver, Colorado 80210, United States*

Thomas P. Gray − *Department of Physics, Department of Chemistry, and JILA, University of Colorado, Boulder, Colorado 80309, United States*

Sean E. Shaheen − *Department of Electrical, Computer, and Energy Engineering, Department of Physics and Renewable and Sustainable Energy Institute, University of Colorado, Boulder, Colorado 80309, United States*

Complete contact information is available at: https://pubs.acs.org/10.1021/acsenergylett.0c00522

Notes

The authors declare no competing financial interest.

■ ACKNOWLEDGMENTS

We thank Omar Khatib and Alex Dixon for their assistance at the early stage of the work for the IR *s*-SNOM measurements and sample preparation, respectively. We also thank Diana-Mari Rossell-Eddy for her assistance in the UV−Vis/photoluminescence measurements. We acknowledge funding from the NSF Science and Technology Center on Real-Time Functional Imaging (STROBE) under DMR-1548924 and from NSF DMR-1906029. J.N. is supported by JSPS Overseas Research Fellowship from the Japan Society for Promotion of Science. A.H.A. thanks Taif University for financial support. We thank the National Renewable Energy Laboratory for use of their facility to prepare the perovskite films.

■ REFERENCES

(1) Kojima, A.; Teshima, K.; Shirai, Y.; Miyasaka, T. Organometal Halide Perovskites as Visible-Light Sensitizers for Photovoltaic Cells. *J. Am. Chem. Soc.* **2009**, *131*, 6050−6051.

(2) Im, J. H.; Lee, C. R.; Lee, J. W.; Park, S. W.; Park, N. G. 6.5% Efficient Perovskite Quantum-Dot-Sensitized Solar Cell. *Nanoscale* **2011**, *3*, 4088−4093.

(3) Lee, M. M.; Teuscher, J.; Miyasaka, T.; Murakami, T. N.; Snaith, H. J. Efficient hybrid solar cells based on meso-superstructured organometal halide perovskites. *Science* **2012**, *338*, 643−647.

(4) Park, N.-G.; Grätzel, M.; Miyasaka, T.; Zhu, K.; Emery, K. Towards stable and commercially available perovskite solar cells. *Nat. Energy* **2016**, *1*, 16152.

(5) Snaith, H. J. Present status and future prospects of perovskite photovoltaics. *Nat. Mater.* **2018**, *17*, 372−376.

(6) Jena, A. K.; Kulkarni, A.; Miyasaka, T. Halide Perovskite Photovoltaics: Background, Status, and Future Prospects. *Chem. Rev.* **2019**, *119*, 3036−3103.

(7) Wasylishen, R. E.; Knop, O.; Macdonald, J. B. Cation rotation in methylammonium lead halides. *Solid State Commun.* **1985**, *56*, 581−582.

(8) Knop, O.; Wasylishen, R. E.; White, M. A.; Cameron, T. S.; Oort, M. J. M. V. Alkylammonium lead halides. Part 2. $CH_3NH_3PbX_3$ (X = Cl, Br, I) perovskites: cuboctahedral halide cages with isotropic cation reorientation. *Can. J. Chem.* **1990**, *68*, 412−422.

(9) Kubicki, D. J.; Prochowicz, D.; Hofstetter, A.; Péchy, P.; Zakeeruddin, S. M.; Grätzel, M.; Emsley, L. Cation Dynamics in Mixed-Cation $(MA)_x(FA)_{1-x}PbI_3$ Hybrid Perovskites from Solid-State NMR. *J. Am. Chem. Soc.* **2017**, *139*, 10055−10061.

(10) Leguy, A. M.; Frost, J. M.; McMahon, A. P.; Sakai, V. G.; Kockelmann, W.; Law, C.; Li, X.; Foglia, F.; Walsh, A.; O'Regan, B. C.; Nelson, J.; Cabral, J. T.; Barnes, P. R. The dynamics of methylammonium ions in hybrid organic-inorganic perovskite solar cells. *Nat. Commun.* **2015**, *6*, 7780.

(11) Frost, J. M.; Walsh, A. What Is Moving in Hybrid Halide Perovskite Solar Cells? *Acc. Chem. Res.* **2016**, *49*, 528−535.

(12) Bakulin, A. A.; Selig, O.; Bakker, H. J.; Rezus, Y. L. A.; Müller, C.; Glaser, T.; Lovrincic, R.; Sun, Z.; Chen, Z.; Walsh, A.; Frost, J. M.; Jansen, T. L. C. Real-Time Observation of Organic Cation Reorientation in Methylammonium Lead Iodide Perovskites. *J. Phys. Chem. Lett.* **2015**, *6*, 3663−3669.

(13) Selig, O.; Sadhanala, A.; Müller, C.; Lovrincic, R.; Chen, Z.; Rezus, Y. L. A.; Frost, J. M.; Jansen, T. L. C.; Bakulin, A. A. Organic Cation Rotation and Immobilization in Pure and Mixed Methylammonium Lead-Halide Perovskites. *J. Am. Chem. Soc.* **2017**, *139*, 4068−4074.

(14) Taylor, V. C. A.; Tiwari, D.; Duchi, M.; Donaldson, P. M.; Clark, I. P.; Fermin, D. J.; Oliver, T. A. A. Investigating the Role of the Organic Cation in Formamidinium Lead Iodide Perovskite Using Ultrafast Spectroscopy. *J. Phys. Chem. Lett.* **2018**, *9*, 895−901.

(15) Gallop, N. P.; Selig, O.; Giubertoni, G.; Bakker, H. J.; Rezus, Y. L.; Frost, J. M.; Jansen, T. L.; Lovrincic, R.; Bakulin, A. A. Rotational Cation Dynamics in Metal Halide Perovskites: Effect on Phonons and Material Properties. *J. Phys. Chem. Lett.* **2018**, *9*, 5987−5997.

(16) Zhu, H.; Miyata, K.; Fu, Y.; Wang, J.; Joshi, P. P.; Niesner, D.; Williams, K. W.; Jin, S.; Zhu, X.-Y. Screening in crystalline liquids protects energetic carriers in hybrid perovskites. *Science* **2016**, *353*, 1409−1413.

(17) Miyata, K.; Atallah, T. L.; Zhu, X.-Y. Lead halide perovskites: Crystal-liquid duality, phonon glass electron crystals, and large polaron formation. *Sci. Adv.* **2017**, *3*, No. e1701469.

(18) Yaffe, O.; Guo, Y.; Tan, L. Z.; Egger, D. A.; Hull, T.; Stoumpos, C. C.; Zheng, F.; Heinz, T. F.; Kronik, L.; Kanatzidis, M. G.; Owen, J. S.; Rappe, A. M.; Pimenta, M. A.; Brus, L. E. Local Polar Fluctuations in Lead Halide Perovskite Crystals. *Phys. Rev. Lett.* **2017**, *118*, 136001.

(19) Nishida, J.; Breen, J. P.; Lindquist, K. P.; Umeyama, D.; Karunadasa, H. I.; Fayer, M. D. Dynamically Disordered Lattice in a Layered Pb-I-SCN Perovskite Thin Film Probed by Two-Dimensional Infrared Spectroscopy. *J. Am. Chem. Soc.* **2018**, *140*, 9882−9890.

(20) Zhu, X.-Y.; Podzorov, V. Charge Carriers in Hybrid Organic−Inorganic Lead Halide Perovskites Might Be Protected as Large Polarons. *J. Phys. Chem. Lett.* **2015**, *6*, 4758−4761.

(21) Bonn, M.; Miyata, K.; Hendry, E.; Zhu, X. Y. Role of Dielectric Drag in Polaron Mobility in Lead Halide Perovskites. *ACS Energy Lett.* **2017**, *2*, 2555−2562.

(22) Munson, K. T.; Swartzfager, J. R.; Asbury, J. B. Lattice Anharmonicity: A Double-Edged Sword for 3D Perovskite-Based Optoelectronics. *ACS Energy Lett.* **2019**, *4*, 1888−1897.

(23) Han, Y.; Meyer, S.; Dkhissi, Y.; Weber, K.; Pringle, J. M.; Bach, U.; Spiccia, L.; Cheng, Y. B. Degradation observations of encapsulated planar $CH_3NH_3PbI_3$ perovskite solar cells at high temperatures and humidity. *J. Mater. Chem. A* **2015**, *3*, 8139−8147.

(24) Yang, J.; Siempelkamp, B. D.; Liu, D.; Kelly, T. L. Investigation of $CH_3NH_3PbI_3$ Degradation Rates and Mechanisms in Controlled Humidity Environments Using in Situ Techniques. *ACS Nano* **2015**, *9*, 1955−1963.
(25) Shirayama, M.; Kato, M.; Miyadera, T.; Sugita, T.; Fujiseki, T.; Hara, S.; Kadowaki, H.; Murata, D.; Chikamatsu, M.; Fujiwara, H. Degradation mechanism of $CH_3NH_3PbI_3$ perovskite materials upon exposure to humid air. *J. Appl. Phys.* **2016**, *119*, 115501.
(26) Li, Z.; Yang, M.; Park, J.-S.; Wei, S.-H.; Berry, J. J.; Zhu, K. Stabilizing Perovskite Structures by Tuning Tolerance Factor: Formation of Formamidinium and Cesium Lead Iodide Solid-State Alloys. *Chem. Mater.* **2016**, *28*, 284−292.
(27) Saliba, M.; Matsui, T.; Seo, J.-Y.; Domanski, K.; Correa-Baena, J.-P.; Nazeeruddin, M. K.; Zakeeruddin, S. M.; Tress, W.; Abate, A.; Hagfeldt, A.; Grätzel, M. Cesium-containing triple cation perovskite solar cells: improved stability, reproducibility and high efficiency. *Energy Environ. Sci.* **2016**, *9*, 1989−1997.
(28) Ghosh, D.; Smith, A. R.; Walker, A. B.; Islam, M. S. Mixed A-Cation Perovskites for Solar Cells: Atomic-Scale Insights Into Structural Distortion, Hydrogen Bonding, and Electronic Properties. *Chem. Mater.* **2018**, *30*, 5194−5204.
(29) Dou, B.; Wheeler, L. M.; Christians, J. A.; Moore, D. T.; Harvey, S. P.; Berry, J. J.; Barnes, F. S.; Shaheen, S. E.; Van Hest, M. F. Degradation of Highly Alloyed Metal Halide Perovskite Precursor Inks: Mechanism and Storage Solutions. *ACS Energy Lett.* **2018**, *3*, 979−985.
(30) Qiao, L.; Sun, X.; Long, R. Mixed Cs and FA Cations Slow Electron−Hole Recombination in $FAPbI_3$ Perovskites by Time-Domain Ab Initio Study: Lattice Contraction versus Octahedral Tilting. *J. Phys. Chem. Lett.* **2019**, *10*, 672−678.
(31) Zhou, L.; Katan, C.; Nie, W.; Tsai, H.; Pedesseau, L.; Crochet, J. J.; Even, J.; Mohite, A. D.; Tretiak, S.; Neukirch, A. J. Cation Alloying Delocalizes Polarons in Lead Halide Perovskites. *J. Phys. Chem. Lett.* **2019**, *10*, 3516−3524.
(32) Tennyson, E. M.; Doherty, T. A. S.; Stranks, S. D. Heterogeneity at multiple length scales in halide perovskite semiconductors. *Nat. Rev. Mater.* **2019**, *4*, 573−587.
(33) Tennyson, E. M.; Garrett, J. L.; Frantz, J. A.; Myers, J. D.; Bekele, R. Y.; Sanghera, J. S.; Munday, J. N.; Leite, M. S. Nanoimaging of Open-Circuit Voltage in Photovoltaic Devices. *Adv. Energy Mater.* **2015**, *5*, 1501142.
(34) Liu, Y.; et al. Chemical nature of ferroelastic twin domains in $CH_3NH_3PbI_3$ perovskite. *Nat. Mater.* **2018**, *17*, 1013−1019.
(35) Yang, M.; Zeng, Y.; Li, Z.; Kim, D. H.; Jiang, C.-S.; van de Lagemaat, J.; Zhu, K. Do grain boundaries dominate non-radiative recombination in $CH_3NH_3PbI_3$ perovskite thin films? *Phys. Chem. Chem. Phys.* **2017**, *19*, 5043−5050.
(36) Leblebici, S. Y.; et al. Facet-dependent photovoltaic efficiency variations in single grains of hybrid halide perovskite. *Nat. Energy* **2016**, *1*, 16093.
(37) Pathoor, N.; Halder, A.; Mukherjee, A.; Mahato, J.; Sarkar, S. K.; Chowdhury, A. Fluorescence Blinking Beyond Nanoconfinement: Spatially Synchronous Intermittency of Entire Perovskite Microcrystals. *Angew. Chem.* **2018**, *130*, 11777−11781.
(38) Correa-Baena, J.-P.; et al. Homogenized halides and alkali cation segregation in alloyed organic-inorganic perovskites. *Science* **2019**, *363*, 627−631.
(39) Jones, T. W.; et al. Lattice strain causes non-radiative losses in halide perovskites. *Energy Environ. Sci.* **2019**, *12*, 596−606.
(40) Stavrakas, C.; Zhumekenov, A. A.; Brenes, R.; Abdi-Jalebi, M.; Bulovic, V.; Bakr, O. M.; Barnard, E. S.; Stranks, S. D. Probing buried recombination pathways in perovskite structures using 3D photoluminescence tomography. *Energy Environ. Sci.* **2018**, *11*, 2846−2852.
(41) El-Hajje, G.; Momblona, C.; Gil-Escrig, L.; Ávila, J.; Guillemot, T.; Guillemoles, J.-F.; Sessolo, M.; Bolink, H. J.; Lombez, L. Quantification of spatial inhomogeneity in perovskite solar cells by hyperspectral luminescence imaging. *Energy Environ. Sci.* **2016**, *9*, 2286−2294.
(42) DeQuilettes, D. W.; Jariwala, S.; Burke, S.; Ziffer, M. E.; Wang, J. T.-W.; Snaith, H. J.; Ginger, D. S. Tracking Photoexcited Carriers in Hybrid Perovskite Semiconductors: Trap-Dominated Spatial Heterogeneity and Diffusion. *ACS Nano* **2017**, *11*, 11488−11496.
(43) Adhyaksa, G. W. P.; Brittman, S.; Āboliņš, H.; Lof, A.; Li, X.; Keelor, J. D.; Luo, Y.; Duevski, T.; Heeren, R. M. A.; Ellis, S. R.; Fenning, D. P.; Garnett, E. C. Understanding Detrimental and Beneficial Grain Boundary Effects in Halide Perovskites. *Adv. Mater.* **2018**, *30*, 1804792.
(44) Delor, M.; Weaver, H. L.; Yu, Q. Q.; Ginsberg, N. S. Imaging material functionality through three-dimensional nanoscale tracking of energy flow. *Nat. Mater.* **2020**, *19*, 56−62.
(45) Sung, J.; Schnedermann, C.; Ni, L.; Sadhanala, A.; Chen, R. Y. S.; Cho, C.; Priest, L.; Lim, J. M.; Kim, H.-K.; Monserrat, B.; Kukura, P.; Rao, A. Long-range ballistic propagation of carriers in methylammonium lead iodide perovskite thin films. *Nat. Phys.* **2020**, *16*, 171.
(46) Tian, W.; Cui, R.; Leng, J.; Liu, J.; Li, Y.; Zhao, C.; Zhang, J.; Deng, W.; Lian, T.; Jin, S. Limiting Perovskite Solar Cell Performance by Heterogeneous Carrier Extraction. *Angew. Chem., Int. Ed.* **2016**, *55*, 13067−13071.
(47) Gross, E. Challenges and opportunities in IR nanospectroscopy measurements of energy materials. *Nano Res.* **2019**, *12*, 2200−2210.
(48) Yuan, Y.; Chae, J.; Shao, Y.; Wang, Q.; Xiao, Z.; Centrone, A.; Huang, J. Photovoltaic Switching Mechanism in Lateral Structure Hybrid Perovskite Solar Cells. *Adv. Energy Mater.* **2015**, *5*, 1500615.
(49) Chae, J.; Dong, Q.; Huang, J.; Centrone, A. Chloride Incorporation Process in $CH_3NH_3PbI_{3-x}Cl_x$ Perovskites via Nanoscale Bandgap Maps. *Nano Lett.* **2015**, *15*, 8114−8121.
(50) Strelcov, E.; Dong, Q.; Li, T.; Chae, J.; Shao, Y.; Deng, Y.; Gruverman, A.; Huang, J.; Centrone, A. $CH_3NH_3PbI_3$ perovskites: Ferroelasticity revealed. *Sci. Adv.* **2017**, *3*, No. e1602165.
(51) Wang, L.; Wang, H.; Wagner, M.; Yan, Y.; Jakob, D. S.; Xu, X. G. Nanoscale simultaneous chemical and mechanical imaging via peak force infrared microscopy. *Sci. Adv.* **2017**, *3*, No. e1700255.
(52) Szostak, R.; Silva, J. C.; Turren-Cruz, S.-H.; Soares, M. M.; Freitas, R. O.; Hagfeldt, A.; Tolentino, H. C. N.; Nogueira, A. F. Nanoscale mapping of chemical composition in organic-inorganic hybrid perovskite films. *Sci. Adv.* **2019**, *5*, No. eaaw6619.
(53) Pollard, B.; Muller, E. A.; Hinrichs, K.; Raschke, M. B. Vibrational nano-spectroscopic imaging correlating structure with intermolecular coupling and dynamics. *Nat. Commun.* **2014**, *5*, 3587.
(54) Muller, E. A.; Pollard, B.; Raschke, M. B. Infrared Chemical Nano-Imaging: Accessing Structure, Coupling, and Dynamics on Molecular Length Scales. *J. Phys. Chem. Lett.* **2015**, *6*, 1275−1284.
(55) Govyadinov, A. A.; Amenabar, I.; Huth, F.; Carney, P. S.; Hillenbrand, R. Quantitative Measurement of Local Infrared Absorption and Dielectric Function with Tip-Enhanced Near-Field Microscopy. *J. Phys. Chem. Lett.* **2013**, *4*, 1526−1531.
(56) Atkin, J. M.; Sass, P. M.; Teichen, P. E.; Eaves, J. D.; Raschke, M. B. Nanoscale Probing of Dynamics in Local Molecular Environments. *J. Phys. Chem. Lett.* **2015**, *6*, 4616−4621.
(57) McLeod, A. S.; Kelly, P.; Goldflam, M. D.; Gainsforth, Z.; Westphal, A. J.; Dominguez, G.; Thiemens, M. H.; Fogler, M. M.; Basov, D. N. Model for quantitative tip-enhanced spectroscopy and the extraction of nanoscale-resolved optical constants. *Phys. Rev. B: Condens. Matter Mater. Phys.* **2014**, *90*, 085136.
(58) Wang, B.; Zhang, Z.-G.; Ye, S.; Rao, H.; Bian, Z.; Huang, C.; Li, Y. Room-temperature water-vapor annealing for high-performance planar perovskite solar cells. *J. Mater. Chem. A* **2016**, *4*, 17267−17273.
(59) Bechtel, H. A.; Muller, E. A.; Olmon, R. L.; Martin, M. C.; Raschke, M. B. Ultrabroadband infrared nanospectroscopic imaging. *Proc. Natl. Acad. Sci. U. S. A.* **2014**, *111*, 7191−7196.
(60) Muller, E. A.; Pollard, B.; Bechtel, H. A.; Blerkom, P. V.; Raschke, M. B. Infrared vibrational nano-crystallography and nano-imaging. *Sci. Adv.* **2016**, *2*, No. e1601006.
(61) Fried, S. D.; Bagchi, S.; Boxer, S. G. Measuring Electrostatic Fields in Both Hydrogen-Bonding and Non-Hydrogen-Bonding Environments Using Carbonyl Vibrational Probes. *J. Am. Chem. Soc.* **2013**, *135*, 11181−11192.

https://dx.doi.org/10.1021/acsenergylett.0c00522
ACS Energy Lett. 2020, 5, 1636−1643

(62) Fried, S. D.; Boxer, S. G. Measuring Electric Fields and Noncovalent Interactions Using the Vibrational Stark Effect. *Acc. Chem. Res.* **2015**, *48*, 998−1006.
(63) Hamm, P.; Zanni, M. T. *Concepts and Methods of 2D Infrared Spectroscopy*; Cambridge University Press, 2011.
(64) Ge, Q. Q.; Ding, J.; Liu, J.; Ma, J. Y.; Chen, Y. X.; Gao, X. X.; Wan, L. J.; Hu, J. S. Promoting crystalline grain growth and healing pinholes by water vapor modulated post-annealing for enhancing the efficiency of planar perovskite solar cells. *J. Mater. Chem. A* **2016**, *4*, 13458−13467.
(65) Xiao, S.; Bai, Y.; Meng, X.; Zhang, T.; Chen, H.; Zheng, X.; Hu, C.; Qu, Y.; Yang, S. Unveiling a Key Intermediate in Solvent Vapor Postannealing to Enlarge Crystalline Domains of Organometal Halide Perovskite Films. *Adv. Funct. Mater.* **2017**, *27*, 1604944.
(66) Wang, P.; Anderson, E. J. D.; Muller, E. A.; Gao, F.; Zhong, Y.; Raschke, M. B. Hyper-spectral Raman imaging correlating chemical substitution and crystallinity in biogenic hydroxyapatite: Dentin and enamel in normal and hypoplastic human teeth. *J. Raman Spectrosc.* **2018**, *49*, 1559−1567.
(67) Nishida, J.; Fayer, M. D. Guest Hydrogen Bond Dynamics and Interactions in the Metal−Organic Framework MIL-53(Al) Measured with Ultrafast Infrared Spectroscopy. *J. Phys. Chem. C* **2017**, *121*, 11880−11890.
(68) Ghosh, D.; Aziz, A.; Dawson, J. A.; Walker, A. B.; Islam, M. S. Putting the Squeeze on Lead Iodide Perovskites: Pressure-Induced Effects to Tune Their Structural and Optoelectronic Behavior. *Chem. Mater.* **2019**, *31*, 4063−4071.
(69) Kubicki, D. J.; Prochowicz, D.; Hofstetter, A.; Zakeeruddin, S. M.; Grätzel, M.; Emsley, L. Phase Segregation in Cs-, Rb- and K-Doped Mixed-Cation $(MA)_x(FA)_{1-x}PbI_3$ Hybrid Perovskites from Solid-State NMR. *J. Am. Chem. Soc.* **2017**, *139*, 14173−14180.
(70) Shannon, R. D. Revised effective ionic radii and systematic studies of interatomic distances in halides and chalcogenides. *Acta Crystallogr., Sect. A: Cryst. Phys., Diffr., Theor. Gen. Crystallogr.* **1976**, *32*, 751−767.
(71) Kieslich, G.; Sun, S.; Cheetham, A. K. Solid-state principles applied to organic−inorganic perovskites: new tricks for an old dog. *Chem. Sci.* **2014**, *5*, 4712−4715.
(72) Alberti, A.; Deretzis, I.; Pellegrino, G.; Bongiorno, C.; Smecca, E.; Mannino, G.; Giannazzo, F.; Condorelli, G. G.; Sakai, N.; Miyasaka, T.; Spinella, C.; Magna, A. L. Similar Structural Dynamics for the Degradation of $CH_3NH_3PbI_3$ in Air and in Vacuum. *ChemPhysChem* **2015**, *16*, 3064−3071.
(73) Wang, Q.; Chen, B.; Liu, Y.; Deng, Y.; Bai, Y.; Dong, Q.; Huang, J. Scaling behavior of moisture-induced grain degradation in polycrystalline hybrid perovskite thin films. *Energy Environ. Sci.* **2017**, *10*, 516−522.
(74) Boyd, C. C.; Cheacharoen, R.; Leijtens, T.; McGehee, M. D. Understanding Degradation Mechanisms and Improving Stability of Perovskite Photovoltaics. *Chem. Rev.* **2019**, *119*, 3418−3451.

https://dx.doi.org/10.1021/acsenergylett.0c00522
ACS Energy Lett. 2020, 5, 1636−1643